2019

Toward Improving Ambient Volta Potential Measurements with SKPFM for Corrosion Studies

Corey M. Efaw
Boise State University

Thiago da Silva
Boise State University

Paul H. Davis
Boise State University

Lan Li
Boise State University

Elton Graugnard
Boise State University

See next page for additional authors

 The archival version of this work was published in *Journal of The Electrochemical Society*, 166(11), C3018-C3027. doi: 10.1149/2.0041911jes.

JES Focus Issue on Electrochemical Techniques in Corrosion Science in Memory of Hugh Isaacs

Toward Improving Ambient Volta Potential Measurements with SKPFM for Corrosion Studies

Corey M. Efaw, Thiago da Silva, Paul H. Davis, Lan Li, Elton Graugnard, and Michael F. Hurley *,z

Micron School of Materials Science and Engineering, Boise State University, Boise, Idaho 83725-2090, USA

Scanning Kelvin probe force microscopy (SKPFM) is used in corrosion studies to quantify the relative nobility of different microstructural features present within complex metallic systems and thereby elucidate possible corrosion initiation sites. However, Volta potential differences (VPDs) measured via SKPFM in the literature for metal alloys exhibit large variability, making interpretation and application for corrosion studies difficult. We have developed an improved method for referencing SKPFM VPDs by quantifying the closely related work function of the probe relative to an inert gold standard whose modified work function is calculated via density functional theory (DFT). By measuring and tracking changes in the probe vs. gold VPD, this method compensates for some of the complex effects that cause changes in an individual probe's work function. Furthermore, it provides a path toward direct, quantitative comparison of SKPFM results obtained by different researchers. Application of this method to a Cu-Ag-Ti eutectic braze of a steel sample imaged with multiple SKPFM probes of differing compositions led to enhanced repeatability both within and among probe types, as well as enabled the calculation of modified work function values for each of the microstructural constituents present.
 [DOI: 10.1149/2.0041911jes]

Manuscript submitted November 1, 2018; revised manuscript received January 4, 2019. Published January 18, 2019. This was Paper 1097 presented at the Seattle, Washington Meeting of the Society, May 13–17, 2018. *This paper is part of the JES Focus Issue on Electrochemical Techniques in Corrosion Science in Memory of Hugh Isaacs.*

The traditional Kelvin probe is a conductive vibrating capacitor-like plate used in vacuum to measure the contact potential difference, which correlates to the work function difference between the probe and the sample of interest. By reducing the size of the Kelvin probe to the nanoscale and combining it with an atomic force microscope (AFM),[1,2] the resulting SKPFM produces simultaneous maps of surface topography and relative Volta potential that correspond to microstructural heterogeneities on the material's surface. Employed under either ambient, inert, or electrolytic environments, SKPFM can spatially resolve features at the nanoscale,[3–5] and has therefore found use in a wide range of diverse applications, including semiconductor[4–7] and electrical device characterization,[8–12] as well as corrosion studies.[13–20]

SKPFM produces nanoscale maps of Volta potential differences (VPD or $\Delta\psi$), which can be calculated theoretically from the difference in work function between the sample surface and the probe (which acts as a pseudo reference), as shown below in Equation 1.[3,21–23]

$$\psi_P^M = \psi^M - \psi^P = \left(\varphi^M - \varphi^P\right)/e \qquad [1]$$

In Equation 1, ψ is Volta potential, ϕ is work function, and e is the elementary charge carried by an electron, while the scripts M and P refer to the (metallic) surface and probe, respectively. Volta potential and work function are surface properties, related to each other by Equation 1 in vacuum conditions. Outside of vacuum, the redefined "modified" work function and Volta potential are measured from the interfaces of the two surfaces and the environment. This recognition of environmental factors having an effect on Volta potential maps has been well established.[3,19,20,24–34] Making the assumption that the interactions between metals M and P and the surface layers from environment are identical, then Equation 1 holds true for non-vacuum conditions.[35]

Further, it is important to note that according to Equation 1, the measured VPD is dependent on the choice of probe and its structural factors. Even the smallest change in the probe, such as degree of structural order (i.e., percent crystallinity), will change the material's work function, and therefore change the measurable VPD.[3] Thus, quantification of the probe's work function in theory can provide repeatable work functions of the features observed from VPD measurements. Though the calculation of the probe's work function is simple in theory, there are many parameters that may influence the probe's work function, especially when mapping Volta potentials at the nanoscale with SKPFM. Most of these parameters are difficult to quantify, including probe wear, aging effects (e.g., oxide growth, hydroxylation, and atmospheric corrosion), reconstruction or relaxation of the probe, and contamination. As a result, comparisons of experimental VPDs derived from SKPFM measurements have been limited to either a pseudo or semi-quantitative scale (e.g., relative nobility in corrosion studies), resulting in large variations in reported VPD values for similar features.[21,36] As a result, alternate routes are used to reliably determine accurate work function values. The overwhelming benefit of SKPFM, however, is that it can provide spatial resolution into the nanoscale. Thus, recent efforts have been made for SKPFM to become a usable technique in highly quantitative spatial mapping of work functions.[4,8,21,22,37]

Though the techniques presented in this work can be used to interpret SKPFM data in many different fields, this work is driven by the desire to further improve the value of SKPFM results in corrosion studies. The Kelvin probe was originally used to observe corrosion properties while the sample was covered with thin electrolyte layers,[38–41] and was increasingly used to study metal alloys with the development of SKPFM. The technique was introduced to the corrosion community when a direct correlation between VPDs and open circuit potentials of metal/electrolyte interfaces was demonstrated.[27,42,43] This was accomplished by comparing Volta potentials of pure metals post-immersion in electrolytic solution to the corrosion potential of the same metal/electrolyte systems. However, the observations between SKPFM measurements and the actual corrosion mechanisms of the material is not directly correlated, as mapping freshly polished metals with the Kelvin probe does not provide direct correlation to corrosion behavior.[3] Electrolyte factors, such as pH and ion concentration, play a major role in the kinetics, which are not addressed when observing fundamental electronic properties of the material in ambient conditions. SKPFM has therefore been utilized for predicting (in ambient or inert conditions) microgalvanic couples as localized corrosion initiation sites for a variety of pristine complex metallic systems,[23,26,28–31,36,44–51] ex situ measurements of such systems following periods of exposure to corrosive environments,[20,52–55] and in situ measurements of VPD changes under non-ambient conditions.[22,23,25,56–61] While much of

*Electrochemical Society Member.
zE-mail: mikehurley@boisestate.edu

the previously reported work has focused on distinguishing relative nobility within individual SKPFM maps, comparisons to other work are not direct. Accordingly, a notable lack of reproducibility in measured VPDs has been observed and discussed for different alloy series.[21,36] This lack of repeatability and an inability to connect to bulk electrochemical testing has led to contradictory conclusions when investigating the corrosion behavior in various metal alloys.[21,22,36,62]

For one route to address this challenge, comparison of calculated work function values for a particular material with the resulting VPDs measured via SKPFM can provide improved predictability of corrosion behavior. Computational chemistry calculations have provided experimentalists with a database of theoretical work function values for various elements. Of recent interest is the ability to increase such a database to microconstituents within complex metal alloys.[21,22,63,64] DFT-based computational simulations[65,66] can show that the crystallographic orientation, as well as the terminating atom of the material surface, can drastically affect the work function.[21,63] Notable shifts in relative VPDs measured via SKPFM have also been linked to metal passivation and/or adsorbed species. This has been confirmed both experimentally[67,68] and by linking experimentation to DFT simulations.[22]

Although DFT simulations can help explain some of the variations seen in measured VPDs, they have only just recently started to address systems that are not perfectly pristine. In reality, following polishing of a material, the surface is actively changing. There are a multitude of factors that can cause this activity, most of which are difficult to quantify, as well as control while doing SKPFM in ambient conditions. Thus, standardization of the SKPFM technique has not been established. This work attempts to control one particular variable for ambient-based SKPFM by directly addressing probe choice and how that contributes to the variability and uncertainty observed in experimentally determined VPDs. Many probe factors, as previously described, will ultimately affect the measured VPD, regardless if active changes are occurring on the surface of the sample. It can thus be seen that the SKPFM probe also likely accounts for some of the variability present in VPDs reported in the literature. However, probe choice, as well as progressive usage of the probe, is commonly removed from SKPFM results by comparing microstructural heterogeneities on the surface to one another.

Recently, redesign of SKPFM probes has been undertaken to address variability in VPD as it is linked to the probe. The redesign is done by applying a coating only to the back side of the probe cantilever, while the tip is left uncoated. The uncoated tip minimizes work function change from tip wear and tip shape. With this redesign, enhanced reproducibility of results has been able to address some of these uncertainties, showing consistent initial VPD results from many probes of the same type.[69]

Though improvements in probe design have resulted in greater consistency during initial probe usage, this work hopes to also address variability in the probe work function from uncontrollable structural variations of probes by utilizing an inert reference material prior to imaging a material of interest. A practice has been presented for SKPFM, wherein the pseudo reference probe is calibrated by comparing Volta potential of the material of interest to the Volta potential of a relatively inert material (e.g., gold).[3,42,52,70,71] Expanding on this approach, the observed work functions of heterogeneities on the surface of metal alloys can be better quantified and ultimately compared to theoretical calculations from DFT. A remarkable agreement between resulting modified work functions of microconstituents calculated using different probes is seen, and thus highlights the utility of this broadly applicable method.

Experimental

SKPFM reference sample.—The inert reference sample employed for this study was a Bruker PFKPFM-SMPL (Santa Barbara, CA), which consists of an n-doped silicon wafer patterned with 50 nm thick rectangular islands of aluminum surrounded by a 50 nm thick interconnect of gold, with small sections of the underlying wafer exposed between the aluminum and gold regions (hereinafter referred to as the Al-Si-Au sample). The abrupt step-wise shifts in VPD from aluminum to silicon to gold can be used to track both inter- and intra-probe consistency, as well as determine SKPFM spatial resolution limitations arising from Volta potential averaging at boundaries by observing the slope of the measured VPD at the transitions between elements of the standard.

Both aluminum and silicon are highly reactive and form passive films when exposed to an ambient environment, thus increasing their surface work functions.[22,67,68] This uncertainty in the physical nature of the aluminum and silicon surfaces of the Al-Si-Au sample could contribute to notable differences between the calculated work functions of the pure materials and the work functions measured experimentally via SKPFM of their oxides. In contrast, gold is a relatively inert metal with expected long-term stability in oxygen-enriched environments (i.e., ambient conditions),[72] and thus should exhibit reasonable agreement between theoretical calculations and experimental measurements. Additional factors such as relative humidity and adsorption of other species will cause changes to the gold surface, which will be assumed to be minimal in ambient air over time. Therefore, work function values of gold were derived using first-principles density functional theory to compare with SKPFM results. X-ray diffraction (XRD) of the Al-Si-Au standard was accomplished using a Rigaku Miniflex 600 X-ray Diffractometer (Tokyo, Japan) to accurately specify the crystallographic orientation of the gold on the standard.

DFT calculations.—Initial atomic structures of gold were built in an FCC crystal structure (space group $Fm\bar{3}m$) with lattice parameters of 4.07 Å.[73] Atomic and electronic structures were calculated using the Vienna ab initio simulation package (VASP)[74] with the projector augmented wave (PAW) method.[75] The Perdew-Burke Ernzerhof (PBE)[76] form of the generalized gradient approximation (GGA)[77] was used for the exchange-correlation potential to address electron-electron interactions. Plane-wave expansion of the wave function was performed with the PAW method and a cutoff energy of 450 eV. Brillouin zone integration was performed on a $9 \times 9 \times 1$ gamma-centered mesh for all the slab structures. Periodic slabs of these structures were built large enough for convergence of the calculated work function and separated by a vacuum of 20 Å to avoid unphysical interactions with neighboring slabs (Figure 1).[84] The vacuum energy level (E_v) and Fermi energy level (E_F) were obtained for each structure, and the theoretical work function (φ) was calculated using Equation 2 below.

$$\varphi = E_v - E_F \quad [2]$$

Work function values for gold were obtained for the (100), (110), and (111) planes to utilize in Equation 1 in quantifying the modified work function of the probe.

SKPFM mapping.—SKPFM was carried out using a Bruker Dimension Icon AFM equipped with a 64 bit NanoScope V controller. Depending upon the precise design characteristics of the probe used for imaging (i.e., spring constant, k, and natural resonance frequency, f_0), two different implementations of SKPFM were employed. Stiffer AFM cantilevers (k on the order of 10s of N/m) utilized single pass tapping mode frequency modulation Kelvin probe force microscopy (FM-KPFM). In this single-pass method, both sample topography and Volta potential are acquired simultaneously. To accomplish this, the probe is mechanically oscillated at or near its natural resonance frequency f_0 (typically 100s of kHz) by a dither piezo while simultaneously a much lower frequency (2 kHz) AC bias is applied to the probe. Variations in the oscillation amplitude at f_0 are used to track changes in the sample topography. Meanwhile, variations in the electric force gradient between the probe and surface, which is modulated at the 2 kHz AC bias frequency, produce sidebands at $f_0 \pm f_{AC}$, with the amplitude of the sidebands proportional to the magnitude of the tip-sample VPD. By applying a variable DC bias to null the sidebands, it becomes possible to measure the tip-sample VPD.[69] Potential inversion is not required when the nullifying bias is applied to the sample,

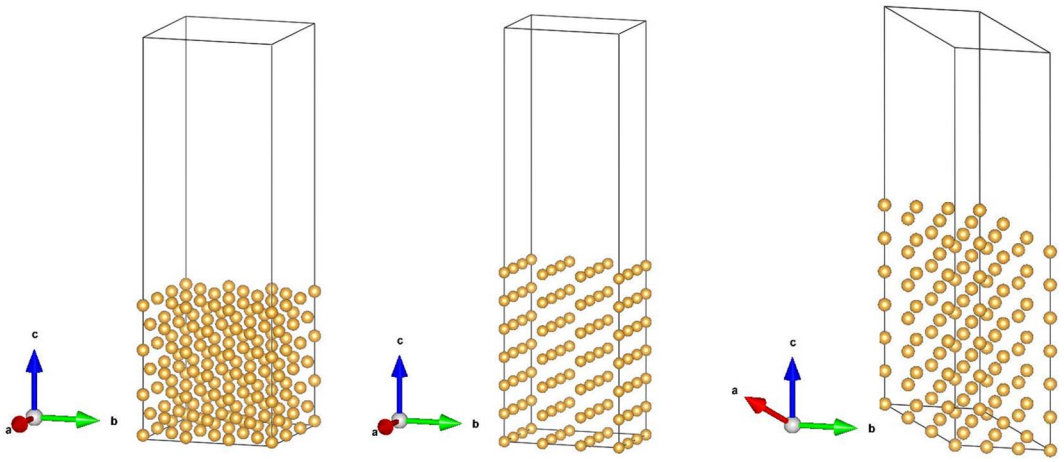

Figure 1. Crystal structures of gold oriented with (from left to right) the (100), (110), and (111) face exposed to vacuum.

and thus the Volta potential of the sample relative to the probe (ψ_P^M) is directly measured. Although the signal-to-noise ratio is lower in FM than in amplitude modulation (AM) technique, it has been shown that the resolution of electric force gradient signal FM surpasses that of AM, and thus was chosen as the method of VPD collection in this work.[69,78] One drawback of FM-KPFM is that the single pass nature is more susceptible to phase cross-talk driven by strong phase contrast.[79]

A second technique, peak force frequency modulation KPFM, or FM PF-KPFM, was employed for softer AFM cantilevers (k on the order of few to tenths of N/m). As the name implies, FM PF-KPFM also utilizes frequency modulation to acquire VPD maps.[69] However, in this implementation the probe conducts a dual pass over the sample surface, wherein line-by-line topography and VPD values are sequentially acquired. In the first pass, sample topography is scanned and recorded using Bruker's proprietary PeakForce tapping mode, which employs rapid (2 kHz) force curve acquisition with a user-defined peak force (5–20 nN in this study) as the setpoint for feedback. Upon completion of each individual trace and retrace line of topography, the probe lifts off the surface and retraces the topography at a user-defined lift height. During the second trace and retrace, VPD measurements are acquired by the frequency modulation method described above for FM TM-KPFM. The lift height has drastic effects on the VPD measurement,[69] and thus a constant lift height (i.e., tip-sample separation) of 100 nm was used throughout this work. Additionally, this lift height will sufficiently avoid artifacts caused by sudden tip-sample contact arising from high aspect ratio features.[37]

SKPFM imaging was performed with three different types of probes: PFQNE-AL (Bruker, $k = 0.8$ N/m, $f_0 = 300$ kHz, 5 nm radius of curvature highly doped silicon tip with an aluminum-based conductive coating on the back side of a silicon nitride cantilever), SCM-PIT (Bruker, $k = 2.8$ N/m, $f_0 = 75$ kHz, 20 nm radius n-doped silicon tip with a conformal platinum/iridium coating covering the cantilever back side and tip), and 25Pt300B (Rocky Mountain Nanotechnology, $k = 18$ N/m, $f_0 = 20$ kHz, 20 nm radius solid platinum probe connected to a conductive gold bonding pad via conductive epoxy). Due to their relatively low spring constants, the PFQNE-AL and SCM-PIT probe types were well-suited to operate in FM PF-KPFM mode, while the solid platinum 25Pt300B probe operated best in the FM-KPFM mode due to its significantly higher spring constant.[69] Temperature was held in the range 68–72 °F, while relative humidity was observed between 5–20%. Variations in VPD results caused by relative humidity and temperature were not accounted for in this work.

Data evaluation.—Image processing and analysis were conducted using NanoScope Analysis V1.8 (Bruker). Threshold analysis, which analyzes the Volta potential channel's data above or below a user-defined value, was implemented as part of the "Roughness" tool in determining VPDs of the heterogeneities in the sample.

Statistical analysis of SKPFM probes was performed by imaging the Al-Si-Au sample to observe variations between probes of both differing and nominally identical composition. SKPFM data on the Al-Si-Au sample were collected and sorted into equidistant VPD "bins", where a higher amount of bins provides higher resolution of data. For all acquired data, 512 bins were used to collect data from each map. The bins collected for each image were placed into populations for each probe type (PFQNE-AL, SCM-PIT, and 25Pt300B), which were each distributed into 512 bins equally dispersed between the maximum and minimum values observed in the population. The population sets for PFQNE-AL, SCM-PIT, and 25Pt300B probes were normalized for variations in data points collected per map, as well as total maps acquired with each probe type. Skewness and 95% confidence interval limits were calculated for each data set. Skewness is a descriptor of the symmetry of a distribution plot, and can quantify the shape of the distribution curves. A symmetric distribution would present a skewness of 0, whereas right and left leaning distributions result in positive and negative skewness values, respectively.

Sample preparation.—Proof of concept SKFPM was performed on a commercial 316L stainless steel coupon separated and thermally re-joined with an active brazing Cu-Ag-Ti alloy (further description of the sample is provided elsewhere).[44] The effect of polishing and sample preparation on VPDs has been previously observed and reported.[67] To minimize effects such as metal passivation and/or adsorbed species on the variability of acquired VPD values, the sample was prepared using the same steps for each map acquisition. To create a fresh, smooth surface for SKPFM, the sample was mechanically ground with progressively finer silicon carbide abrasive pads to US 1200 grit. Following SiC grinding, the sample was polished with 1 μm and 0.05 μm alumina slurries. Following each polishing step, the sample was sequentially rinsed with DI water and non-denatured 190-proof ethanol, then dried with compressed air. Following polishing and immediately prior to SKPFM imaging, the sample was cleaned by ultrasonication in ethanol, then dried with compressed ultrahigh purity (UHP) nitrogen gas (99.999%, Norco). An electrical connection between the sample surface and the AFM stage was then established using colloidal silver paint (PELCO®) and verified with a digital voltmeter. The Al-Si-Au sample was mapped both prior to and following mapping of the braze sample to ensure consistency of the probe for the entirety of the imaging session, as well as provide calculation of the work functions of the constituents seen on the braze surface.

The elemental distribution of the Cu-Ag-Ti brazed stainless steel sample was determined by a Hitachi S-3400N-II scanning electron microscope (SEM) equipped with energy-dispersive X-ray spectroscopy (EDS) capabilities (Oxford Instruments Energy+, Oxford Instruments, Abingdon, United Kingdom) operated at 10 keV and a 10 mm working distance. Due to the residual effects of electron

Table I. Density functional theory calculated work function values for gold over relevant planes.

Material	Face	Vacuum Energy E_v	Fermi Energy E_F	Work Function φ	Ref. (Approx.)
Gold	(100)	4.770 eV	−0.324 eV	5.09 eV	5.0–5.2 eV[81-83]
	(110)	2.590 eV	−2.410 eV	5.00 eV	
	(111)	3.357 eV	−1.759 eV	5.12 eV	

beam irradiation and carbon pyrolysis, all SEM/EDS mapping was performed after SKPFM measurements.[36,47,80]

Results and Discussion

DFT calculated work functions.—The work functions of three different possible exposed faces of pure gold were determined via DFT calculations. Table I summarizes the results, which are in agreement with those reported in the literature.[81–83] XRD results from the Al-Si-Au standard showed a dominant peak of gold in the (111) orientation. From these results, 5.12 eV was used as the calculated work function of the gold on the standard.

Quantifying probe work function.—Prior to utilizing the described method to quantify the work functions of the constituents present in the braze sample, an experiment was conducted to quantify statistical differences between probe types, as well as between probes of the same design. To accomplish this, mapping of the Al-Si-Au sample was done twelve times (in a successive manner so as to minimize drastic variations in temperature and relative humidity during testing) with eight different probes (three PFQNE-AL, three SCM-PIT, and two 25Pt300B), for a total of 96 SKPFM maps of the Al-Si-Au sample. Representative VPD maps of the standard obtained with each probe type are shown in Figure 2a–2c.

Variability between probe types.—Figure 2d presents the average VPDs (with standard deviations) obtained from all data for each of the three probe types relative to the gold standard. From Equation 1, the VPD between the probe and gold (ψ_P^{Au}) measured via SKPFM is equivalent to the difference in work function between the gold surface (φ^{Au}, calculated by DFT to be 5.12 eV, Table I) and the probe (φ^P). By multiplying the VPD, ψ_P^{Au}, by a negative magnitude of electron charge and then adding the work function of gold, the modified work function of the probe can be found. For the population results for each probe type, the average modified work function of each probe type can be found (right ordinate axis in Figure 2d).

For ambient air SKPFM, the results show that the PFQNE-AL and SCM-PIT probes exhibit relative precision for a large population of data, with lower standard deviations (246 mV and 106 mV, respectively) combined with low skewness values of +0.18 and +0.47. The 25Pt300B probe also shows a relatively symmetric distribution (skewness of −0.29), but produces a much larger range of VPD values (standard deviation >700 mV, Figure 2d). This may be due to the use of the single-pass tapping mode that the 25Pt300B probe employs, as well as the conflation caused by interactions between the surface and the entirety of the probe, which is composed entirely of platinum. Confidence intervals at 95% for each set are provided in Figure 2e, and show that the three probe types exhibit statistically significant differences in VPD versus gold, and therefore statistically different average probe modified work functions. The probe types exhibiting different modified work functions is as expected, given their differing material compositions. Thus, VPDs measured via SKPFM on the same alloy with these different probe types will be offset by the corresponding differences in probe work function.

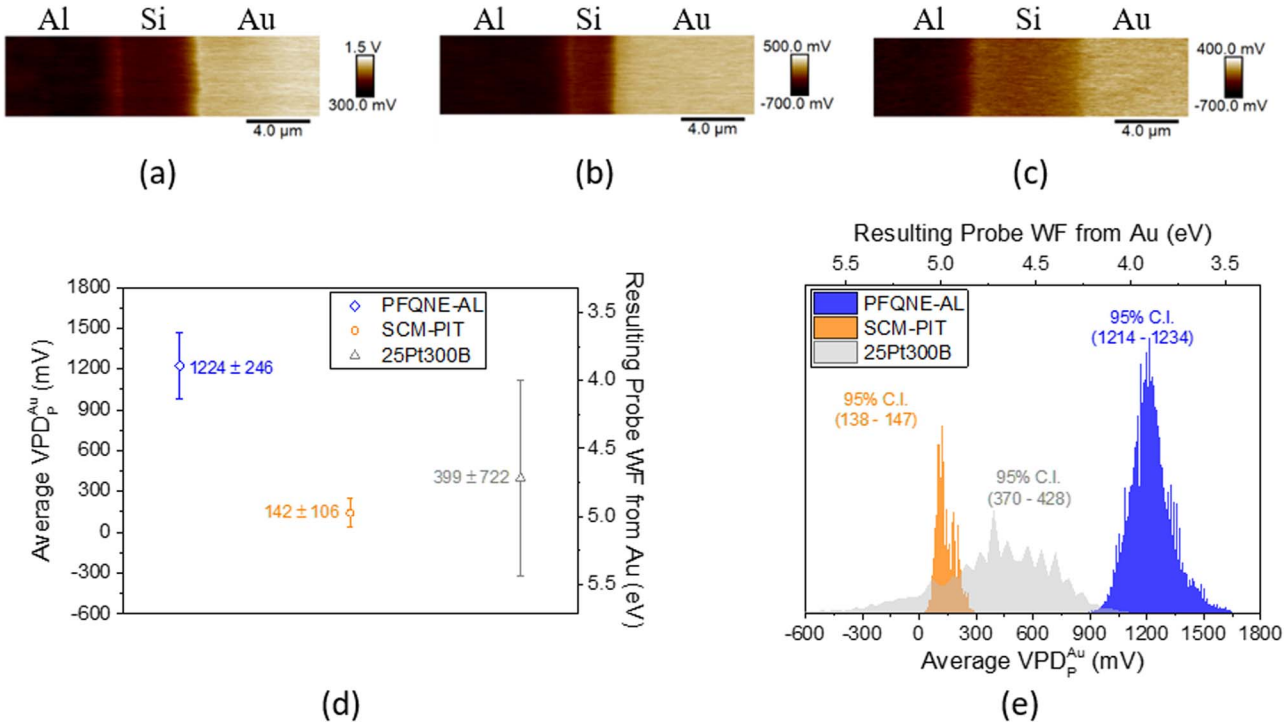

Figure 2. Representative SKPFM VPD maps of the Al-Si-Au standard obtained with (a) a PFQNE-AL probe, (b) a SCM-PIT probe, and (c) a 25Pt300B probe. Note the difference in VPD color scale ranges for panels (a-c) due to differences in probe work functions. (d) Average gold VPD acquired from all SKPFM images obtained with each probe type. Left ordinate axis presents the average VPDs (with standard deviations) measured between the gold and the given probe type (PFQNE-AL in blue, SCM-PIT in orange, 25Pt300B in gray). Right ordinate axis presents the resulting average modified work function calculated for each probe type. (e) VPD and modified work function distributions of gold acquired from all SKPFM images with each probe type, with respective axes presented below and above the distributions. 95% confidence intervals are presented beside each histogram.

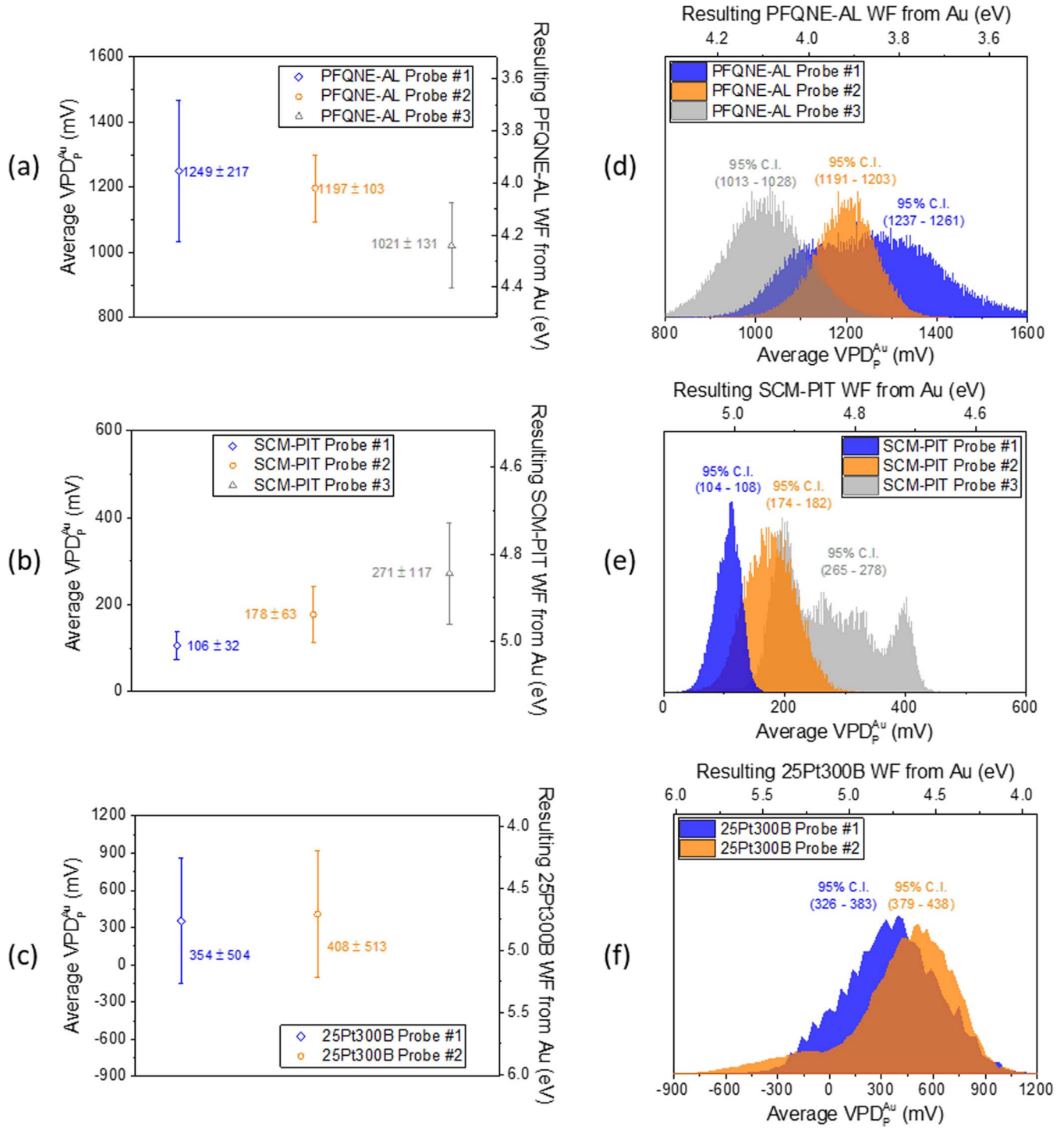

Figure 3. (Left) Average gold VPDs (with standard deviations) obtained from twelve SKPFM images acquired on the Al-Si-Au standard with (a) three PFQNE-AL probes, (b) three SCM-PIT probes, and (c) two 25Pt300B probes. Left ordinate axes present the average VPDs measured between the gold and the given probe. Right ordinate axes present the resulting average work function calculated for each of the probes. (Right) Distributions of measured VPDs for gold and resultant modified probe work functions obtained from twelve SKPFM images with (d) three PFQNE-AL probes, (e) three SCM-PIT probes, and (f) two 25Pt300B probes. 95% confidence intervals are presented besides each histogram.

Variability of individual probes by type.—The data obtained from the twelve images collected with each of the eight individual probes tested (i.e., 8 data sets made by the 12 SKPFM images acquired by the individual probes) were further statistically analyzed and compared to each other to determine the distribution of intra-probe variability. Figure 3 presents variations between individual probes of the same type, both as averages (with standard deviations) in Figures 3a–3c and as histograms in Figures 3d–3f. Similar statistical analyses were performed on the data for each individual probe as described above for the aggregate data for each probe type (i.e., observation of 'Probe A' in the previous section, observation of 'Probe A1', 'Probe A2', and 'Probe A3 in this section). The data from each of the eight individual probes exhibited relatively symmetric distributions, with skewness values for all distributions $<|0.75|$. There is one distinct

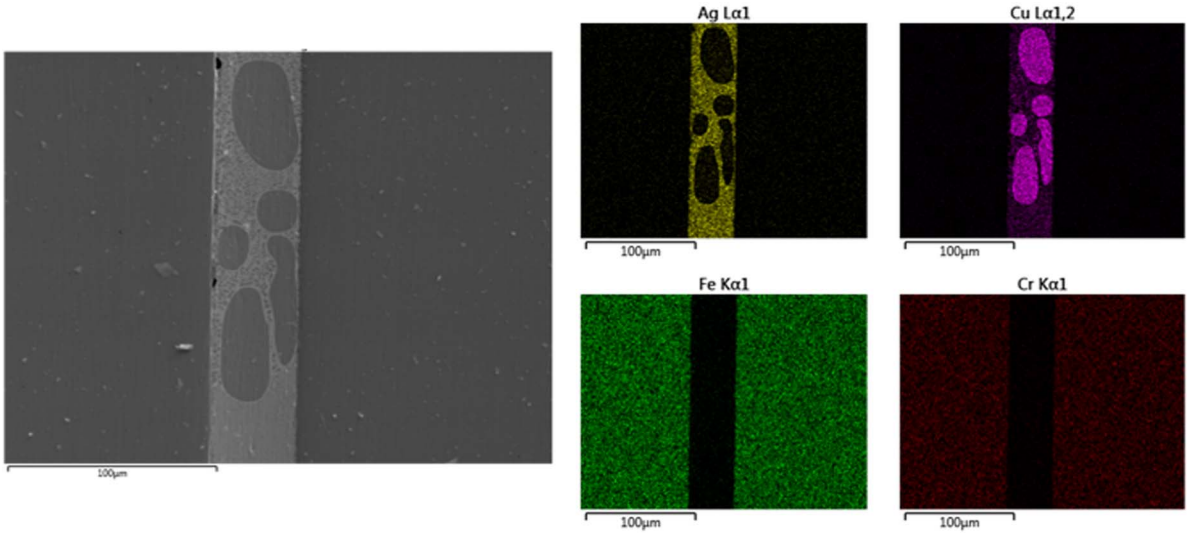

Figure 4. Grayscale SEM image (left) and colored EDS maps (right) of the Cu-Ag-Ti brazed 316L stainless steel sample, confirming the presence of two distinct phases within the braze material: copper-rich precipitates within a silver-rich braze matrix.

probe showing either bimodal (PFQNE-AL Probe #1) or multimodal (SCM-PIT Probe #3) histograms. These probes are still useful for collecting semi-quantitative or qualitative VPD results of individual maps (e.g., relative nobility). However, if improved accuracy of work function calculations are desired, these probes lack consistent, predictable use. Also, confidence intervals for the PFQNE-AL and the SCM-PIT probes are not overlapping (Figures 3d–3e). The confidence intervals for the two 25Pt300B probes do overlap (Figure 3f); however, their standard deviations are vastly larger (Figure 3c) than for the other two probe types. This suggests a larger range of VPDs could be measured on a given sample with the 25Pt300B probe type, and thus it is less reliable for repeatable work function calculations. In addition, the statistically significant differences observed between probes of the same make-up and design highlights the need for probe quantification prior to SKPFM imaging of a material of interest to enable comparison of VPD measurements made with different probes, even of the same type. The bimodal and multimodal behavior of specific probes also suggests shifting in probe work function over time and usage, driven by other factors such as environmental changes over time (e.g., relative humidity and temperature) and structural changes of the probe as previously described. SKPFM still has validity in the corrosion field (e.g. semi-quantitative analysis, relative nobility, effects of environment, etc.) as proven by the number of works done by others. However, greater control of outside parameters will be needed to further the improved standardization of the technique, as well as improve the precision of work function calculations. Though many other parameters are not precisely controlled, this statistical study still shows that the constant monitoring of probe work function is required, particularly when used in ambient conditions.

Relative work functions of different metallic constituents.—Once the probe's work function has been quantified by mapping the inert gold portion of the Al-Si-Au sample, the SKPFM data acquired from the sample of interest (in this case, a Cu-Ag-Ti braze sample) can be placed on an absolute scale. Elemental mapping of the Cu-Ag-Ti braze region with SEM/EDS revealed a two-phase eutectic structure of copper-rich regions embedded within a silver-rich matrix, with titanium (a wetting agent) diffusing to the braze-steel interface (Figure 4).[44] Thus, two distinct phases can be readily distinguished on the surface of the sample – a copper-rich phase (Cu-rich) and a silver-rich phase (Ag-rich). Note that micro-segregation is still evident in this sample, meaning that each phase is rich in a certain element, but is still alloyed. This brazing material presents near-pure metals to validate to well-known elemental work function values, but exhibits enough complexity as an alloy to show expansion from pure material observations. Thus, SKPFM mapping is done within the Cu-Ag-Ti braze material to observe differences between the two phases.

Figure 5 shows VPD maps acquired with the three different probe types, all of whose modified work functions were quantified using the inert gold of the Al-Si-Au sample immediately before imaging the braze sample. It is notable that the results acquired by the different probe types show differing lateral resolution, in order of superiority (least to highest) from 25Pt300B to SCM-PIT to PFQNE-AL probe type. This can be attributed to a combination of the technique used (single pass tapping mode versus dual pass PF- FM KPFM), as well as probe design and resultant resolution (i.e., contributions from both the tip and the cantilever causing a decrease in lateral resolution for the 25Pt300B and SCM-PIT relative to the PFQNE-AL, which is only coated on the back side). All images acquired on the braze alloy have pixel resolution between 24–28 nm. However, regardless of resolution, the SKPFM maps obtained with all three probe types present consistent relative nobility within the braze area, wherein the silver-rich braze matrix is noble relative to the copper-rich regions. This confirms the utility of SKPFM for assessing relative nobility of the sample's constituents. From this, a microgalvanic couple is distinguished, and atmospheric corrosion behavior can be predicted. To expand SKPFM use toward acquiring consistent modified work functions of the two phases in the sample, probe quantification relative to an inert material is needed. As shown in Figure 6a, the resulting VPD values for each phase vs. probe are notably different.

Figures 6b–6c presents the method quantifying the probe relative to gold as a reference prior to imaging the braze sample. Figure 6b presents the average VPD of gold from the Al-Si-Au sample versus each probe. Utilizing Equation 1, the resulting probe modified work function can be calculated, as shown on the right ordinate axis and the equation below Figure 6b. In Figure 6c, displayed on the left ordinate axis (as well as the equation above Figure 6c) is the VPD of each phase relative to the VPD of gold mapped with the probes just prior to mapping the braze sample. Another way to display the results can be seen on the right ordinate axis, where each phase's absolute modified work function is calculated via the equation shown below Figure 6c. In this case, the gold from the Al-Si-Au sample is used as reference to quantify the work function of the operating probe, as previously described. Following quantification of probe work function, Equation 1 can again be used to calculate the work function of each phase present on the braze sample, where the average VPD between the specific phase and probe (ψ_P^M) is found from the potential map, and probe modified work function (φ^P) is found in Figure 6b. From this,

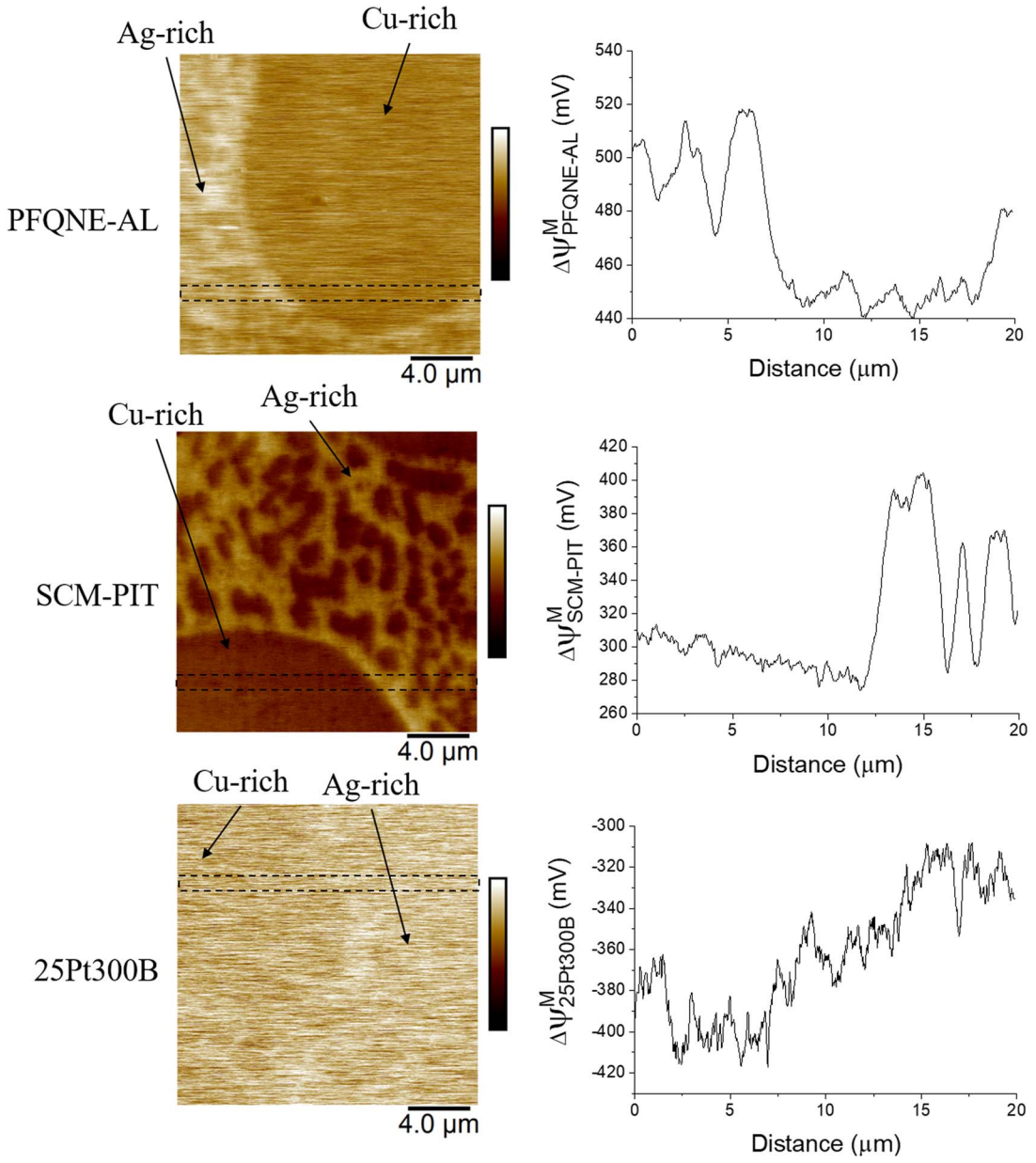

Figure 5. SKPFM (VPD) maps and cross sections of the Cu-Ag-Ti braze sample acquired with a PFQNE-AL probe (500 mV scale), a SCM-PIT probe (500 mV scale), and a 25Pt300B probe (800 mV scale). Cu-rich and Ag-rich phases are called out in each map. Cross sections correspond to average data across the dotted black areas.

the distribution of plausible results for each of the phases has been reduced from a range of >800 mV (Figure 6a), to a range of <150 mV (or alternatively <0.15 eV in modified work functions, Figure 6c).

Since probes of the same type can also exhibit differences in their modified work function, the same process was used to analyze images acquired with different probes of the same type. The PFQNE-AL probe was chosen for this experiment. Figure 7 presents SKPFM images (VPD maps) captured by two different PFQNE-AL probes on different dates at different locations within the braze sample. For further comparison, a third VPD map has been presented in a previous publication[44] and is analyzed here as well. Parameters for these acquired data were similar to parameters described in this work. Figure 8a displays the VPD of each phase determined from the three separate SKPFM images. Again, although the relative nobility is consistent, the three separate tests conducted on this material by probes of the same nominal composition result in three vastly different measured VPD values. Using the method outlined in this work, the resulting distribution for the Cu-rich and Ag-rich regions reduces the average VPD range from >700 mV (Figure 8a) to <55 mV (or alternatively <0.055 eV, Figure 8c), thereby demonstrating the power and utility of this method.

Conclusions

This work proposes a methodology for presenting SKPFM VPD results by utilizing a relatively inert reference material (gold) to enable determination of the absolute modified work function of materials, as opposed to merely the relative difference in Volta potential between the sample and non-equilibrated, pseudo-reference probe. Implementing this simple addition to standard SKPFM practice could greatly reduce the notable variation in reported VPDs for heterogeneities seen in metallic alloys that can arise from differences in probe type/composition, variability between individual probes of a given type, and/or changes in probe work function over time.

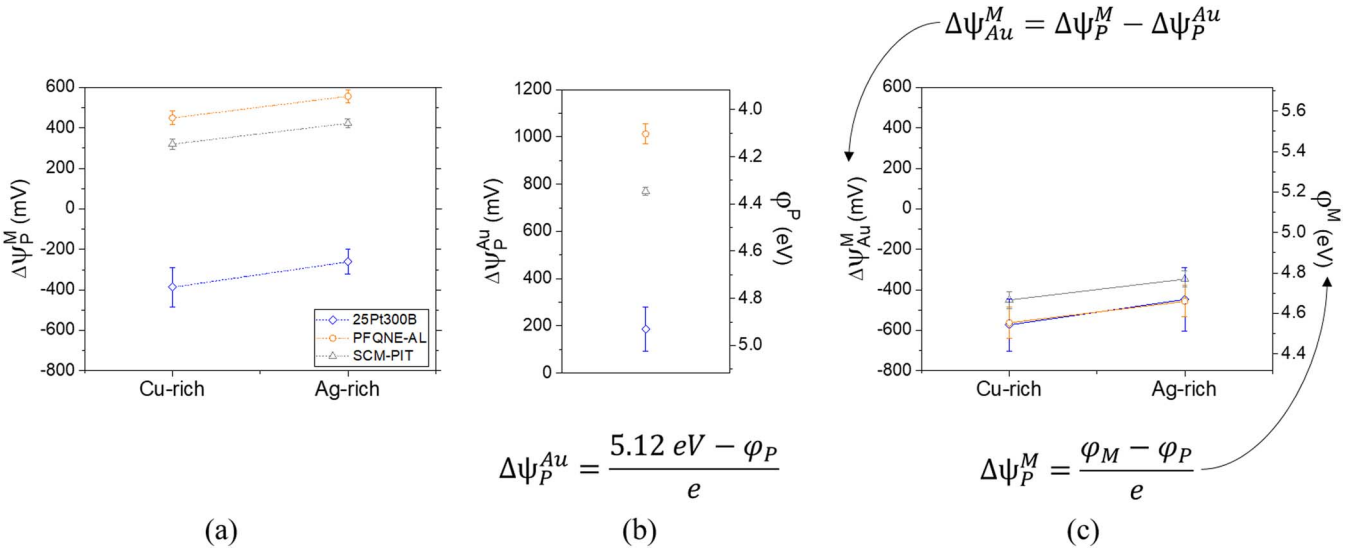

Figure 6. (a) VPD results for copper-rich and silver-rich regions on the braze sample obtained with the three different probe types as seen in Figure 5b VPD results for the same three probes acquired from the gold of the Al-Si-Au standard presented on the left ordinate axis, with resulting modified probe work function values presented on the right ordinate axis, as calculated with the shown equation. (c) VPDs scaled relative to the gold of the Al-Si-Au standard imaged with the same probe prior to imaging the braze sample. The left ordinate axis (as calculated by the equation above) scales the VPD between the phases of the braze sample and the gold of the standard. The right ordinate axis (as calculated by the equation below) presents the resultant modified work function for each phase based on the modified work function of the probe in part (b).

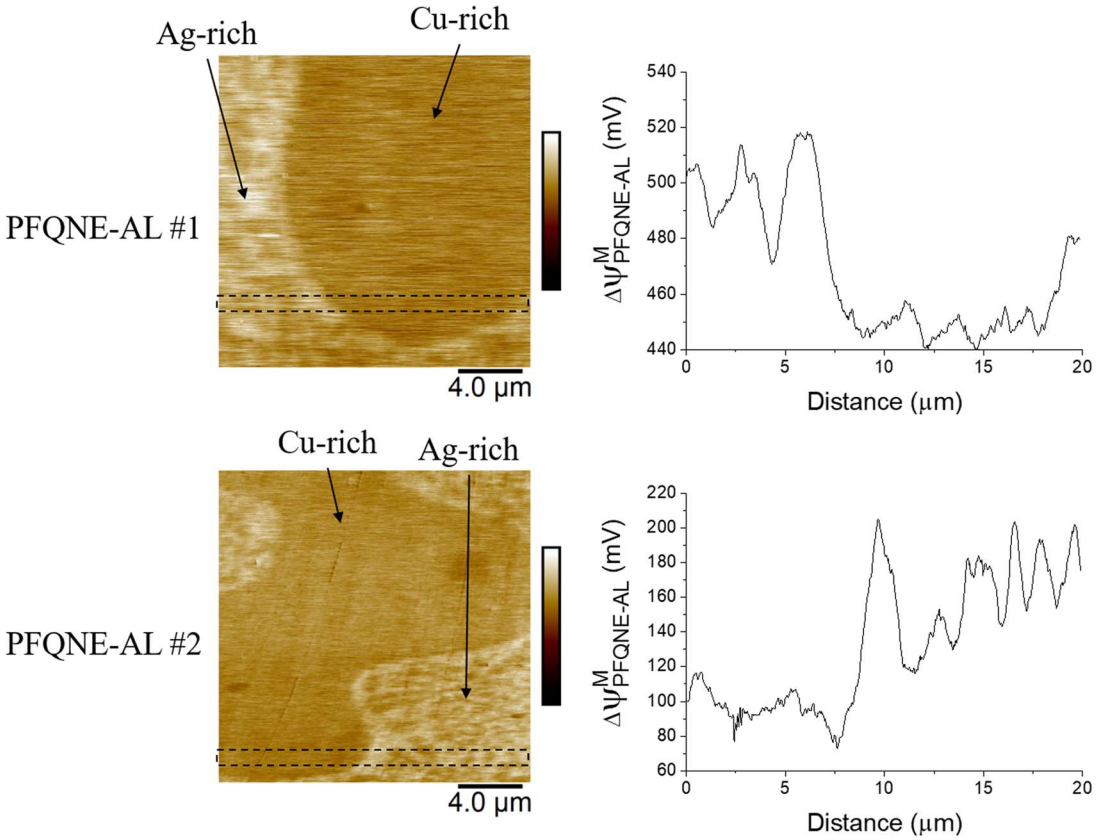

Figure 7. SKPFM (VPD) maps and cross sections of the Cu-Ag-Ti braze sample obtained with different PFQNE-AL probes. PFQNE-AL #1 is a duplicate of Figure 5, while PFQNE-AL #2 (600 mV scale) is from a different region of braze sample with a different probe. Cross sections coordinate to average data across the dotted black areas.

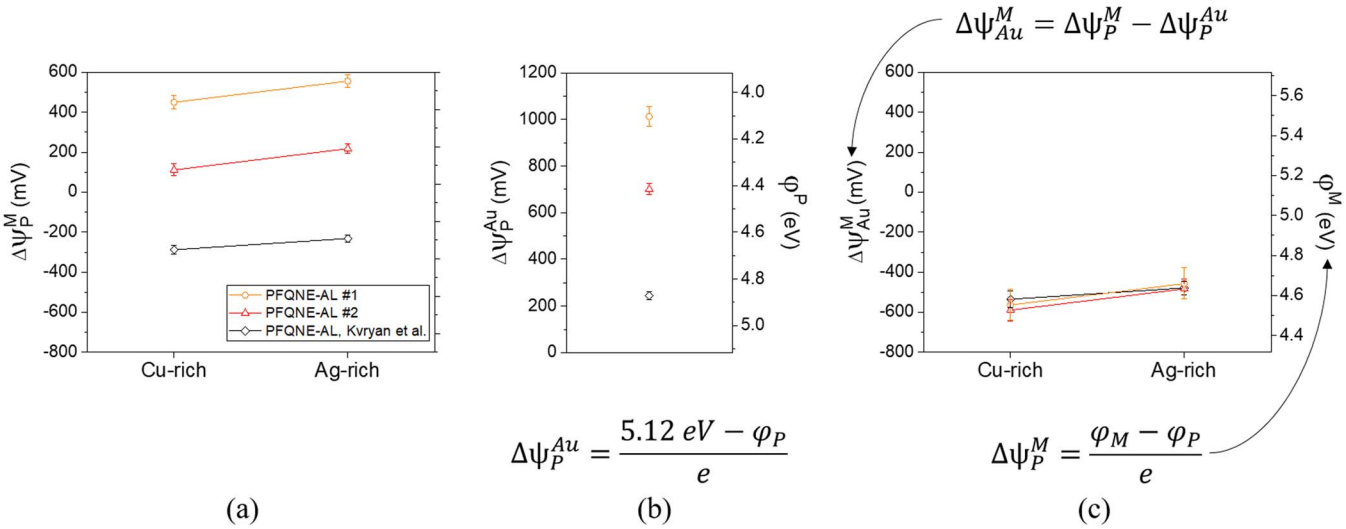

Figure 8. (a) VPD results for copper-rich and silver-rich regions on the braze sample obtained with three different PFQNE-AL probes as seen in Figure 7 and from Kvryan et al.[44] (b) VPD results for the same three probes acquired from the gold of the Al-Si-Au standard presented on the left ordinate axis, with resulting modified PFQNE-AL work function values presented on the right ordinate axis, as calculated with the shown equation. (c) VPDs scaled relative to the gold of the Al-Si-Au standard imaged prior to imaging of the braze sample. The left ordinate axis (as calculated by the equation above) scales the VPD between the phases of the braze sample and the gold of the standard. The right ordinate axis (as calculated by the equation below) presents the resultant modified work function for each phase based on the modified work function of the probe in part (b).

The utility of this method was demonstrated by quantifying the statistically significant differences in VPDs and work functions between probes of different types and among probes of the same type, as well as changes in VPD over time for a given probe. Using the Cu-Ag-Ti braze sample as an example, the spread of measured VPDs was greatly reduced regardless of probe used for the testing. With the support of DFT calculations, SKPFM can provide nanoscale spatially resolved work functions. With knowledge of the operating probe's relative work function, various heterogeneities seen on common metal alloys can be cataloged and compared to DFT modeled predictions. By advancing DFT efforts to more complex multicomponent systems, as well as improving the repeatability and standardization of SKPFM, a connection between theory and experimentation can start to form. By bridging the gap between these two regions of focus, an improved understanding of materials beyond single element make-up can occur. Additionally for corrosion studies, the improved standardization of SKPFM will enable a greater understanding of the driving force behind corrosion initiation and progression on the nanoscale.

Acknowledgments

CME, and MFH acknowledge funding from the NASA Idaho Space grant Consortium EPSCoR Seed Grant. Computing facilities (TdS and LL) were provided by Boise State University's R1 and R2 computing clusters as well as Idaho National Laboratory's high performance computing center. The authors thank the Boise State Center for Materials Characterization and Surface Science Laboratory staff for experimental assistance and access to their instrumentation resources.

ORCID

Paul H. Davis https://orcid.org/0000-0001-7333-8748
Elton Graugnard https://orcid.org/0000-0002-0497-9821
Michael F. Hurley https://orcid.org/0000-0001-6324-4350

References

1. M. Nonnenmacher, M. P. Oboyle, and H. K. Wickramasinghe, *Appl Phys Lett*, **58**(25), 2921 (1991).
2. J. M. R. Weaver and D. W. Abraham, *J Vac Sci Technol B*, **9**(3), 1559 (1991).
3. M. Rohwerder and F. Turcu, *Electrochim Acta*, **53**(2), 290 (2007).
4. S. Sadewasser, T. Glatzel, S. Schuler, S. Nishiwaki, R. Kaigawa, and M. C. Lux-Steiner, *Thin Solid Films*, **431**, 257 (2003).
5. F. Krok, K. Sajewicz, J. Konior, M. Goryl, P. Piatkowski, and M. Szymonski, *Phys Rev B*, **77**(23), 235427 (2008).
6. Y. Leng, C. C. Williams, L. C. Su, and G. B. Stringfellow, *Appl Phys Lett*, **66**(10), 1264 (1995).
7. S. Sadewasser, P. Jelinek, C. K. Fang, O. Custance, Y. Yamada, Y. Sugimoto, M. Abe, and S. Morita, *Phys Rev Lett*, **103**(26), (2009).
8. N. J. Lee, J. W. Yoo, Y. J. Choi, C. J. Kang, D. Y. Jeon, D. C. Kim, S. Seo, and H. J. Chung, *Appl Phys Lett*, **95**(22), 222107 (2009).
9. H. Hoppe, T. Glatzel, M. Niggemann, A. Hinsch, M. C. Lux-Steiner, and N. S. Sariciftci, *Nano Lett*, **5**(2), 269 (2005).
10. S. C. Nagpure, B. Bhushan, and S. S. Babu, *J Power Sources*, **196**(3), 1508 (2011).
11. S. Sadewasser, N. Nicoara, and S. D. Solares, *Beilstein J Nanotech*, **9**, 1272 (2018).
12. O. M. Slobodian, P. M. Lytvyn, A. S. Nikolenko, V. M. Naseka, O. Y. Khyzhun, A. V. Vasin, S. V. Sevostianov, and A. N. Nazarov, *Nanoscale Res Lett*, **13** (2018).
13. P. Campestrini, E. P. M. van Westing, H. W. van Rooijen, and J. H. W. de Wit, *Corros Sci*, **42**(11), 1853 (2000).
14. F. Andreatta, H. Terryn, and J. H. W. de Wit, *Corros Sci*, **45**(8), 1733 (2003).
15. F. Andreatta, H. Terryn, and J. H. W. de Wit, *Electrochim Acta*, **49**(17-18), 2851 (2004).
16. C. Larignon, J. Alexis, E. Andrieu, L. Lacroix, G. Odemer, and C. Blanc, *Electrochim Acta*, **110**, 484 (2013).
17. C. Ornek and D. L. Engelberg, *J Mater Sci*, **51**(4), 1931 (2016).
18. C. Ornek, J. Walton, T. Hashimoto, T. L. Ladwein, S. B. Lyon, and D. L. Engelberg, *J Electrochem Soc*, **164**(6), C207 (2017).
19. Y. Yan, H. J. Yang, Y. J. Su, and L. J. Qiao, *Electrochem Commun*, **64**, 61 (2016).
20. T. Y. Pan, *J Appl Electrochem*, **42**(12), 1049 (2012).
21. Y. Jin, M. Liu, C. H. Zhang, C. Leygraf, L. Wen, and J. S. Pan, *J Electrochem Soc*, **164**(9), C465 (2017).
22. C. Ornek, M. Liu, J. Pan, Y. Jin, and C. Leygraf, *Top Catal*, **61**(9-11), 1169 (2018).
23. A. P. Nazarov and D. Thierry, *Electrochim Acta*, **49**(17-18), 2955 (2004).
24. G. S. Frankel, M. Stratmann, M. Rohwerder, A. Michalik, B. Maier, J. Dora, and M. Wicinski, *Corros Sci*, **49**(4), 2021 (2007).
25. O. Ozkanat, B. Salgin, M. Rohwerder, J. M. C. Mol, J. H. W. de Wit, and H. Terryn, *J Phys Chem C*, **116**(10), 6505 (2012).
26. F. N. Afshar, J. H. W. de Wit, H. Terryn, and J. M. C. Mol, *Electrochim Acta*, **88**, 330 (2013).
27. A. B. Cook, Z. Barrett, S. B. Lyon, H. N. McMurray, J. Walton, and G. Williams, *Electrochim Acta*, **66**, 100 (2012).
28. J. X. Jia, A. Atrens, G. Song, and T. H. Muster, *Mater Corros*, **56**(7), 468 (2005).
29. J. H. W. de Wit, *Electrochim Acta*, **49**(17-18), 2841 (2004).
30. N. Sathirachinda, R. Pettersson, and J. S. Pan, *Corros Sci*, **51**(8), 1850 (2009).
31. N. Sathirachinda, R. Pettersson, S. Wessman, U. Kivisakk, and J. S. Pan, *Electrochim Acta*, **56**(4), 1792 (2011).
32. R. F. Schaller and J. R. Scully, *Electrochem Commun*, **40**, 42 (2014).
33. R. F. Schaller and J. R. Scully, *Electrochem Commun*, **63**, 5 (2016).
34. A. Davoodi, J. Pan, C. Leygraf, and S. Norgren, *Electrochim Acta*, **52**(27), 7697 (2007).
35. A. Frumkin and A. Gorodetzkaja, *Z Phys Chem-Stoch Ve*, **136**(6), 451 (1928).

36. M. F. Hurley, C. M. Efaw, P. H. Davis, J. R. Croteau, E. Graugnard, and N. Birbilis, *Corrosion-Us*, **71**(2), 160 (2015).
37. W. Melitz, J. Shen, A. C. Kummel, and S. Lee, *Surf Sci Rep*, **66**(1), 1 (2011).
38. M. Stratmann, *Corros Sci*, **27**(8), 869 (1987).
39. M. Stratmann and H. Streckel, *Corros Sci*, **30**(6-7), 697 (1990).
40. M. Stratmann and H. Streckel, *Corros Sci*, **30**(6-7), 681 (1990).
41. M. Stratmann, H. Streckel, K. T. Kim, and S. Crockett, *Corros Sci*, **30**(6-7), 715 (1990).
42. P. Schmutz and G. S. Frankel, *J Electrochem Soc*, **145**(7), 2285 (1998).
43. V. Guillaumin, P. Schmutz, and G. S. Frankel, *J Electrochem Soc*, **148**(5), B163 (2001).
44. A. Kvryan, K. Livingston, C. M. Efaw, K. Knori, B. J. Jaques, P. H. Davis, D. P. Butt, and M. F. Hurley, *Metals-Basel*, **6**(4), 91 (2016).
45. A. E. Coy, F. Viejo, P. Skeldon, and G. E. Thompson, *Corros Sci*, **52**(12), 3896 (2010).
46. L. Vieira, F. L. C. Lucas, S. F. Fisssmer, L. C. D. dos Santos, M. Massi, P. M. S. C. M. Leite, C. A. R. Costa, E. M. Lanzoni, R. S. Pessoa, and H. S. Maciel, *Surf Coat Tech*, **260**, 205 (2014).
47. C. F. Mallinson, A. Harvey, and J. F. Watts, *J Electrochem Soc*, **164**(7), C342 (2017).
48. N. Birbilis, K. Meyer, B. C. Muddle, and S. P. Lynch, *Corros Sci*, **51**(8), 1569 (2009).
49. F. N. Afshar, A. M. Glenn, J. H. W. de Wit, H. Terryn, and J. M. C. Mol, *Electrochim Acta*, **104**, 48 (2013).
50. A. Alvarez-Pampliega, Y. Gonzalez-Garcia, K. Van den Bergh, J. De Strycker, and H. Terryn, *Mater Corros*, **66**(1), 16 (2015).
51. R. Arrabal, B. Mingo, A. Pardo, E. Matykina, M. Mohedano, M. C. Merino, A. Rivas, and A. Maroto, *Corros Sci*, **97**, 38 (2015).
52. P. Schmutz and G. S. Frankel, *J Electrochem Soc*, **145**(7), 2295 (1998).
53. K. H. Anantha, C. Ornek, S. Ejnermark, A. Medvedeva, J. Sjostrom, and J. S. Pan, *J Electrochem Soc*, **164**(4), C85 (2017).
54. M. Sarvghad-Moghaddam, R. Parvizi, A. Davoodi, M. Haddad-Sabzevar, and A. Imani, *Corros Sci*, **79**, 148 (2014).
55. Q. F. Yu and T. Y. Pan, *Metall Mater Trans A*, **48A**(5), 2618 (2017).
56. A. Nazarov, V. Vivier, D. Thierry, F. Vucko, and B. Tribollet, *J Electrochem Soc*, **164**(2), C66 (2017).
57. G. Back, A. Nazarov, and D. Thierry, *Corrosion-Us*, **61**(10), 951 (2005).
58. M. Jonsson, D. Thierry, and N. LeBozec, *Corros Sci*, **48**(5), 1193 (2006).
59. A. Nazarov, N. Le Bozec, and D. Thierry, *Prog Org Coat*, **114**, 123 (2018).
60. A. Nazarov, N. Le Bozec, D. Thierry, P. Le Calve, and J. P. Pautasso, *Corrosion-Us*, **68**(8), 720 (2012).
61. A. Nazarov, F. Vucko, and D. Thierry, *Electrochim Acta*, **216**, 130 (2016).
62. L. Lacroix, L. Ressier, C. Blanc, and G. Mankowski, *J Electrochem Soc*, **155**(1), C8 (2008).
63. D. Q. Sun, Y. X. Wang, Y. L. Lu, Z. Chen, and Q. L. Rao, *Superlattice Microst*, **94**, 215 (2016).
64. H. Lu, Z. R. Liu, X. G. Yan, D. Y. Li, L. Parent, and H. Tian, *Sci Rep-Uk*, **6** (2016).
65. W. Kohn and L. J. Sham, *Phys Rev*, **137**(6A), 1697 (1965).
66. P. Hohenberg and W. Kohn, *Phys Rev B*, **136**(3B), B864 (1964).
67. B. S. Tanem, G. Svenningsen, and J. Mardalen, *Corros Sci*, **47**(6), 1506 (2005).
68. K. A. Yasakau, A. N. Salak, M. L. Zheludkevich, and M. G. S. Ferreira, *J Phys Chem C*, **114**(18), 8474 (2010).
69. C. Li, S. Minne, Y. M. Hu, J. He J., H. Mittel, V. Kelly, N. Erina, S. Guo, and T. Mueller, *in* "Bruker Application Note #140", p. 1–14. Bruker Nano Surfaces Division, 2013.
70. P. Leblanc and G. S. Frankel, *J Electrochem Soc*, **149**(6), B239 (2002).
71. C. Ornek and D. L. Engelberg, *Corros Sci*, **99**, 164 (2015).
72. W. M. Sachtler, G. J. H. Dorgelo, and A. A. Holscher, *Surf Sci*, **5**(2), 221 (1966).
73. E. R. Jette and F. Foote, *J Chem Phys*, **3**(10), 605 (1935).
74. G. Kresse and J. Furthmuller, *Phys Rev B*, **54**(16), 11169 (1996).
75. G. Kresse and D. Joubert, *Phys Rev B*, **59**(3), 1758 (1999).
76. J. P. Perdew, K. Burke, and M. Ernzerhof, *Phys Rev Lett*, **77**(18), 3865 (1996).
77. J. P. Perdew and W. Yue, *Phys Rev B*, **33**(12), 8800 (1986).
78. J. Colchero, A. Gil, and A. M. Baro, *Phys Rev B*, **64**(24), (2001).
79. C. Li, S. Minne, Y. Hu, J. Ma, J. He, H. Mittel, V. Kelly, N. Erina, S. Guo, and T. Mueller, *in* "Bruker Application Note #140", p. 1–14. Bruker Nano Surfaces Division, 2013.
80. C. F. Mallinson and J. F. Watts, *J Electrochem Soc*, **163**(8), C420 (2016).
81. D. Cornil and J. Cornil, *J Electron Spectrosc*, **189**, 32 (2013).
82. A. S. Hyla, P. Winget, H. Li, C. Risko, and J. L. Bredas, *Org Electron*, **37**, 263 (2016).
83. N. E. Singh-Miller and N. Marzari, *Phys Rev B*, **80**, 235407 (2009).
84. K. Momma and F. Izumi, *J. Appl. Crystallogr*, **44**, 1272 (2011).